Ultrathin quasi-perfect absorber for low-frequency and broadband underwater sound

Yanni Zhang [a,], Jie Pan [b], Kean Chen [a], Zhaoyu Wei [c], Jie Zhong [d]

[a] *School of Marine Science and Technology, Northwestern Polytechnical University, Xi'an, Shaanxi, 710072, China*

[b] *School of Engineering, the University of Western Australia, Perth, Western Australia, 6009, Australia*

[c] *Institute of Oceanography, Shanghai Jiao Tong University, Shanghai, 200240, China*

[d] *Laboratory of Science and Technology on Integrated Logistics Support, National University of Defense Technology, Changsha, Hunan, 410073, China*

We proposed an ultrathin absorber that can efficiently absorb broadband and quasi-omnidirectional underwater sound. The absorber consists of a thin viscoelastic (VE) layer embedded with thin-plate scatterers (PSs) of equal width but with gradient variation in thickness. A dynamic model considering the full interaction of the PSs as a thin plate and the VE matrix as an elastic solid is used to predict the absorption coefficient of the absorber, which is validated by an effective medium model and the finite element model. The absorber exhibits perfect or quasi-perfect absorption (QPA) in multiple bands and broad incident angles at deep subwavelength thickness, due to resonant excitation of multiple local modes of different types in the absorber. By properly adjusting the absorbers' geometric and the material properties, broadband QPAs of over 99%, 95%, and 90% at bandwidths of 202.0 Hz, 348.3 Hz, and 572.9 Hz, respectively, are achieved via combined effects of multiple locally resonant (LR) modes. It thus offers an effective method for controlling low-frequency and broadband underwater sound.

*Corresponding author.
Email address: yanni.zhang@nwpu.edu.cn

1. Introduction

Effective absorption of low-frequency and broadband sound has always been a challenging task, especially for underwater sound, which has a longer wavelength than sound in air at the same frequency. This is because of the weak intrinsic dissipation of sound waves with longer wavelengths by traditional viscoelastic (VE) materials [1, 2]. High/perfect sound absorption (SA) can only be realized if the thickness of the absorbing material is no less than a quarter-wavelength (QW) of the longitudinal waves in the material or a QW of the incident sound for sound in air [3]. To enhance low-frequency SA capabilities, various methods have been proposed, including multi-layered structures [4], a rigid or heavy elastic backing [5, 6], impedance gradient coatings [7], embedding cavity resonators [8, 9], and usage of ceramic foam [10]. However, the first three methods inevitably make the absorber bulky or heavy. Embedding cavities, despite being lightweight, suffer from large deformation at high hydrostatic water pressure and may have reduced effect [2, 11]. On the other hand, ceramic foams, which demonstrate high low-frequency absorption, require heavy backing behind the sample.

The discovery of the local resonance (LR) principle opens a new path for controlling

low-frequency noise by light, subwavelength structures [12–14]. Typical local resonators consist of softly coated heavy spheres embedded in a hard matrix [12, 13]. High absorption is thus achieved at the LR frequency, which is adjustable by varying the effective mass and stiffness. However, the bandwidth of the absorption peak is still too narrow, even considering dissipation. To overcome this, placing multiple resonators with a single degree-of-freedom into one unit cell was proposed to broaden the working bandwidth by increasing the number of SA peaks at different frequencies [15–17]. To realize a broadband effect, more resonators must be introduced, thus increasing the weight of the structure, yet the performance is still limited. Efficiently broadening the bandwidth of low-frequency SA remains a challenge.

Recently, perfect/quasi-perfect acoustic absorbers of subwavelength thickness or of low weight have become a focus of research [1, 18–24], including those using Helmholtz resonators [18–20], QW resonators [20], an acoustic membrane absorber [1, 21], a lossy-resonant plate absorber [22], and a labyrinthine acoustic absorber [3, 23, 24]. Despite these studies for airborne sound, few perfect or quasi-perfect absorbers have been reported for water-borne sound and in the presence of transverse waves, although a quasi-perfect absorption of water-borne sound has been observed by Mei *et al.* [24] by a metasurface whose thickness is only 0.15 times the wavelength of the absorbed sound. Broadband perfect/quasi-perfect absorption for underwater sound at a subwavelength range is still a challenge.

Recently, by embedding multiple elastic plate scatterers (PSs) into a unit cell of a VE matrix layer, we observed perfect and quasi-perfect absorptions at multiple frequencies or in a broad band [25] corresponding to a deep subwavelength regime of incident sound. In each unit cell, these multiple elastic PSs of equal thickness but gradiently varying widths, were distributed uniformly along the z-direction and parallel to the layer surfaces. In this work, a quasi-perfect absorber is proposed via a different structural configuration. The absorber is made up of a VE matrix layer inserted with multiple elastic PSs of equal width but gradually varied thickness in a unit cell. Results show that the proposed absorber can also achieve perfect/quasi-perfect absorption at multiple LR frequencies and a broad band below the QW frequency. The effects of geometrical parameters, including the thickness, thickness gradient, and width of the PSs, and the thickness of and loss factors related to elastic waves in the VE layer are also discussed. It is also shown, by considering embedded PSs with the same total weight, that the current absorber exhibits lower LR frequencies compared with the absorber in Ref. [25], yet the current one is relatively easier to fabricate, making it a simpler and efficient device for absorbing low-frequency and broadband underwater sound. The effects of the intrinsic loss factors of elastic waves in the VE layer on the broadband SA behavior of the absorber are also discussed.

2. Description of the sound absorber

The sound absorber proposed in this paper consists of a VE layer embedded with a set of elastic PSs, as schematically shown in Fig. 1. The density and thickness of the VE layer/absorber are respectively ρ_1 and h_1. The upper and lower half-spaces of the absorber are water and air, respectively. In each unit cell, I elastic PSs of width L, thickness h_{2i}, and density ρ_2 are distributed uniformly along the z-direction and parallel to the surfaces of the layer, where $i = 1, 2, 3, \ldots, I$, with I an integer greater than 1. Thus, the distance between the PSs in a unit $h_{c1} = h_1/(I+1)$. The thickness of the ith PS, h_{2i}, is gradiently varied as $h_{2i} = h_{2I} + (6 - i)\Delta_h$ with

Δ_h the thickness gradient. The lattice constant is l and the distance between the units of PSs is d.

A plane acoustic wave is impinging upon the absorber with an incident angle θ_i and amplitude P_i. The sound wavenumber in water is $k_o = \omega/c_o$, with c_o the related sound speed and ω the angular frequency. The blocked pressure is calculated from the incident pressure and its specular reflection $p_b(x,z) = 2P_i \cos(k_o(z - Ih_{c1})\cos\theta_i)e^{-jk_o x \sin\theta_i}$. The sound scattered by and that transmitted through the absorber is due to sound radiation from the upper and lower surfaces of the absorber excited by the blocked pressure.

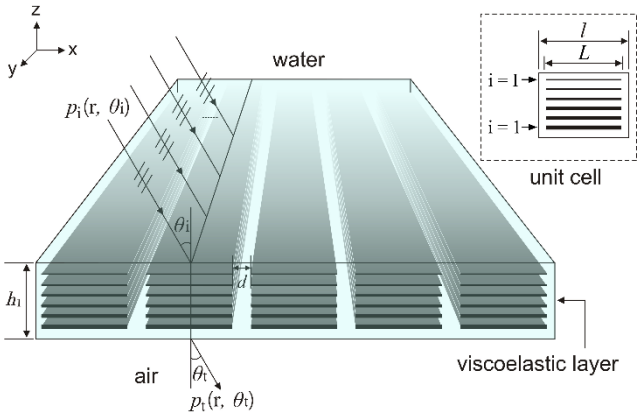

Fig. 1. Schematic diagram of the proposed sound absorber.

3. Theoretical modeling and analytical solution

3.1. Dynamic model

The SA properties of the proposed absorber are simulated using a dynamic model (DM) based on an analytical modelling of the interaction between the PSs and the VE layer, similar to what was established in Ref. 25. Briefly, both the scattered sound pressure P_s and the transmitted sound pressure P_t in the upper and lower fluids satisfy the 2D sound wave equation in the x and z planes. The elastic waves in the VE layer satisfy the 2D wave equation in an elastic solid [26–28]. Classical plate theory (CPT) is applied for the description of motion of each PS, which are thin compared with the thickness of the VE layer and the wavelength of shear waves in the PSs [25, 29]. With all constraints directly exerted on the neutral plane of each PS, the force equilibrium and displacement continuity in both normal and shear directions at all interface surfaces are thus given by:

1) At $z = -h_{c1}$:

$$\frac{1}{\rho_a \omega^2}\frac{\partial p_t(x,z)}{\partial z}\bigg|_{z=-h_{c1}} = u_z^{(1)}(x,-h_{c1}), \tag{1}$$

$$\sigma_z^{(1)}(x,-h_{c1}) = -p_t(x,-h_{c1}), \text{ and} \tag{2}$$

$$\tau_{zx}^{(1)}(x,-h_{c1}) = 0; \tag{3}$$

2) At $z = (i-1)h_{c1}$:

$$\sigma_z^{(i)}\left(x,(i-1)h_{c1}\right)-\sigma_z^{(i+1)}\left(x,(i-1)h_{c1}\right)=\frac{h_{2i}}{2}\sum_{n=-\infty}^{+\infty}\left[\frac{\partial\tau_{zx}^{(i)}\left(x,(i-1)h_{c1}\right)}{\partial x}+\frac{\partial\tau_{zx}^{(i+1)}\left(x,(i-1)h_{c1}\right)}{\partial x}\right]$$

$$\cdot\Delta H_n(x)+\left[\rho_2 h_{2i}\omega^2\sum_{n=-\infty}^{+\infty}\Delta H_n(x)-\sum_{n=-\infty}^{+\infty}\frac{\partial^2}{\partial x^2}\left(D_{2i}\Delta H_n(x)\frac{\partial^2}{\partial x^2}\right)\right]u_z^{(i)}\left(x,(i-1)h_{c1}\right) \quad (4)$$

$$\tau_{zx}^{(i)}\left(x,(i-1)h_{c1}\right)-\tau_{zx}^{(i+1)}\left(x,(i-1)h_{c1}\right)=$$

$$\sum_{n=-\infty}^{+\infty}\left[\frac{\partial}{\partial x}\left(E_{2i}^{'}\Delta H_n(x)\frac{\partial}{\partial x}\right)+\rho_2 h_{2i}\omega^2\Delta H_n(x)\right]\left[u_x^{(i)}\left(x,(i-1)h_{c1}\right)-\frac{h_{2i}}{2}\frac{\partial u_z^{(i)}\left(x,(i-1)h_{c1}\right)}{\partial x}\right], \quad (5)$$

$$u_z^{(i)}\left(x,(i-1)h_{c1}\right)-u_z^{(i+1)}\left(x,(i-1)h_{c1}\right)=0\text{, and} \quad (6)$$

$$u_x^{(i)}\left(x,(i-1)h_{c1}\right)-u_x^{(i+1)}\left(x,(i-1)h_{c1}\right)=ih_{2i}\sum_{n=-\infty}^{+\infty}\frac{\partial u_z^{(i)}\left(x,(i-1)h_{c1}\right)}{\partial x}\Delta H_n(x)\text{;} \quad (7)$$

3) At $z = Ih_{c1}$:

$$\sigma_z^{(I+1)}(x,Ih_{c1})=-p_b(x,Ih_{c1})-p_s(x,Ih_{c1})\text{,} \quad (8)$$

$$\tau_{zx}^{(I+1)}(x,Ih_{c1})=0\text{, and} \quad (9)$$

$$u_z^{(I+1)}(x,Ih_{c1})=\frac{1}{\rho_o\omega^2}\frac{\partial p_s(x,z)}{\partial z}\Big|_{z=Ih_{c1}}\text{;} \quad (10)$$

where $D_{2i}=\frac{E_2h_{2i}^3}{12(1-\nu_2)}$ and $E_{2i}^{'}=\frac{E_2h_{2i}}{(1-\nu_2)}$, with $i = 1, 2, 3, \ldots, I$, and $\Delta H_n(x)=H(x-nl-l/2)-H(x-nl+l/2)$ defines the position of the PSs in the nth unit cell, with $n=0,\pm1,\pm2,\ldots$.

The displacement, stress, and pressure components in Eqs. (1)–(10) can be expanded as:

$$u_r^{(i)}(x,z)=\sum_{m=-\infty}^{+\infty}U_{rm}^{(i)}(z)e^{-jk_mx}\text{,} \quad (11)$$

$$\tau_{zr}^{(i)}(x,z)=\sum_{m=-\infty}^{+\infty}F_{rm}^{(i)}(z)e^{-jk_mx} \quad (12)$$

$$p_s(x,z)=\sum_{m=-\infty}^{+\infty}P_{sm}e^{-jk_mx-\gamma_m(z-Ih_{c1})}\text{, for } z\geq Ih_{c1}\text{, and} \quad (13)$$

$$p_t(x,z)=\sum_{m=-\infty}^{+\infty}P_{tm}e^{-jk_mx+\eta_m(z+h_{c1})}\text{, for } z\leq -h_{c1}\text{,} \quad (14)$$

where $r = z$ or x represent the normal or shear components, respectively; $k_m=k_o\sin\theta_i+2\pi m/l$ and m are the numbers of space harmonics; $U_{zm}^{(i)}(z)$, $U_{xm}^{(i)}(z)$, $F_{zm}^{(i)}(z)$, and $F_{xm}^{(i)}(z)$ are equivalent to their counterparts in Ref. [27] with α_m, β_m, ρ_1, and c_s invariant with i; $P_{sm}=-\rho_0\omega^2/\gamma_mU_{zm}^{(2)}(Ih_{c1})$ and $P_{tm}=\rho_a\omega^2/\eta_mU_{zm}^{(1)}(-h_{c1})$ according to Eqs. (1) and (10);

$\gamma_m = \sqrt{k_m^2 - k_o^2}$ and $\eta_m = \sqrt{k_m^2 - k_a^2}$ are the sound wavenumbers in the *z*-direction in the upper and lower half-spaces, respectively; and $k_a = \omega / c_a$ is the sound wavenumber in air.

$\Delta H_n(x)$ in Eqs. (4)–(7) can also be expanded as a sum of Fourier series as

$$\sum_{n=-\infty}^{+\infty} \Delta H_n(x) = \sum_{n=-\infty}^{+\infty} c_n e^{-j2n\pi x/l}, \text{ where } c_n = \begin{cases} e^{-jn\pi L/l}(e^{j2n\pi L/l} - 1) / j2n\pi, n \neq 0 \\ L/l, \qquad\qquad n = 0 \end{cases}. \quad (15)$$

By substituting Eqs. (11)–(15) into Eqs. (1)–(10) and using the orthogonality of the space harmonics in a spatial period, the *q*-indexed coefficient equations are produced:

$$[C_q]\{\mathrm{x}_q\} + \sum_{n=-\infty}^{+\infty} [\mathrm{F}_{n,q-n}]\{\mathrm{x}_n\} = \{\mathrm{p}_q\}, \quad (16)$$

where $[C_q]$ and $\{\mathrm{p}_q\}$ are equivalent to their counterparts in Ref. 25; $[\mathrm{F}_{n,q-n}]$ is a $(4I+4)\times(4I+4)$ matrix different from that in Ref. 25 with its entries listed in the Appendix; and $\{\mathrm{x}_q\} = [A_q^{(2i+1)}, B_q^{(2i+1)}, A_q^{(2i+2)}, B_q^{(2i+2)}, \ldots A_q^{(2I+1)}, B_q^{(2I+1)}, A_q^{(2I+2)}, B_q^{(2I+2)}]^{\mathrm{T}}$ for $i = 0, 1, 2, 3, \ldots, I$, are the unknown wave propagation coefficients of the *q*th mode.

By rewriting Eq. (16) in global matrix form (̂ , ̂ ,̂ for all values of the index *q*, the solution ̂ ⋯ ⋯ can be expressed as:

̂ , ̂ , (17)

where ̂ , ̂ , and ̂ are in the same forms as their counterparts in Ref. [25]. Note that, although ̂ as a block-partitioned matrix is in the same form as those derived in Refs. [25], [26], and [27], its entries related to multiple PSs in a unit are completely different from those due to one single PS in each unit cell in Refs. [26] and [27] and are also different from those in Ref. [25] due to PSs with equal thicknesses but gradiently varied widths.

The total surface pressure and surface velocity are thus calculated by:

$$p_T(x, Ih_{c1}) = p_b(x, Ih_{c1}) + p_s(x, Ih_{c1}) \quad (18)$$

and:

$$v_z^I(x, Ih_{c1}) = j\omega u_z^I(x, Ih_{c1}). \quad (19)$$

The SA coefficient over one period length *l* of the surface is given by:

$$\alpha = \Pi_{ab} / \Pi_{in}, \quad (20)$$

where $\Pi_{ab} = -\frac{1}{2} Re\{\int_0^l p_T(x, Ih_{c1}) v_z^{I*}(x, Ih_{c1}) dx\}$ and $\Pi_{in} = l\frac{|P_i|^2 \cos(\theta_i)}{2\rho_0 c_0}$ are respectively the absorbed and incident sound powers (*i.e.*, the sound powers per unit length in the *y*-direction)

over l, where *Re* denotes the real part of a complex value and the asterisk denotes the complex conjugate.

3.2. Equivalent medium model

An equivalent medium model (EMM) based on the transfer matrix method is presented to validate the results at a long-wavelength range when the dilatational wavelength in the VE matrix $\lambda_{d1} >> l$, L, and h_2. Each layer containing the ith PS can be regarded as a homogeneous layer, with an equivalent characteristic impedance denoted as Z_{ei}. Since the CPT is applied to each PS, whose thickness deformation is neglected, all constraints are directly exerted on the neutral plane of each PS. Thus, Z_{ei} is directly related to the characteristic impedance of each PS Z_{pi} by $Z_{ei} = Z_{pi} \times f_r$, where $f_r = L/l$ and $Z_{pi} = j\rho_2 c_{d2} \tan(k_{d2} h_{2i})$, with c_{d2} and $k_{d2} = \omega / c_{d2}$ the longitudinal wave velocity and the related wavenumber of the PS, respectively. Note that, in the low-frequency range and for a thin PS, $Z_{pi} \cong j\rho_2 h_{2i} \omega$.

The characteristic impedance of layer i can then be calculated using the well-known transmission line theory as:

$$Z^e_{2i+1} = Z_{d1} \frac{Z^e_{2i} + jZ_{d1} \tan(k_1 h_{c1})}{jZ^e_{2i} \tan(k_1 h_{c1}) + Z_{d1}}, i = 0,1,2,3,..,I \ , \tag{21}$$

where $Z_{d1} = \rho_1 c_{d1}$ and $Z^e_{2i} = Z_{ei} + Z^e_i$, with $Z^e_0 \simeq$. The normal absorption coefficient (AC) based on the EMM can thus be calculated as $\alpha = 1 - |r_p|^2$, with the reflection coefficient $r_p = (Z^e_{2I+1} - \rho_0 c_0) / (Z^e_{2I+1} + \rho_0 c_0)$.

4. Numerical model

A finite-element model (FEM) is also developed using COMSOL Multiphysics® (v5.1) to verify the proposed analytical model. The VE matrix is modeled as a solid domain and the water and air are modeled as acoustic fluid domains. Each embedded PS is modeled as a solid element based on the theory of elasticity. Only a unit cell of the absorber is modeled, due to its spatial periodicity. A periodic boundary condition is applied on the boundaries of the unit cell in the x-direction. At the interface of the PS and solid matrix domain, the stress equilibrium and displacement continuity in both the normal and tangential directions are applied. A fully coupled acoustic–structure boundary condition is applied at the interface of the solid and fluid domains. Perfectly matched layers are added at both the top of the water domain and the bottom of the air domain to mimic anechoic termination of outgoing waves [30]. The reflected and transmitted pressures through the layer were measured at the upper- and lower-side boundaries of the layer, respectively. The AC can then be calculated by:

$$\alpha = 1 - R_I - T_I, \tag{22}$$

where $R_I = \left(|p_r| / |p_i| \right)^2$ and $T_I = Z_w \left(|p_t| / |p_i| \right)^2 / Z_a$, with $Z_w = \rho_w c_w / \cos(\theta_i)$ and $Z_a = \rho_a c_a / \cos(\theta_t)$ the normal impedances of the water and air, respectively.

5. Results and discussion

For simulation, the material and geometric parameters adopted for the absorber are as follows: $\rho_0 = 1000$ kg/m^3 and $c_0 = 1500$ m/s for water; $h_1 = 6$ cm, $\rho_1 = 400$ kg/m^3, $c_{d1} = 550\sqrt{1} + j0.05$ m/s, and $c_{s1} = 50\sqrt{1} + j0.3$ m/s for the VE layer; $h_{2l} = 1.5$ mm, $\Delta_h = 0.1$ mm, $\rho_2 = 7800$ kg/m^3, $E_2 = 216$ GPa, $\nu_2 = 0.3$, and $\eta = 0.001$ for each embedded PS; and $\rho_a = 1.21$ kg/m^3 and $c_a = 340$ m/s for air. Since the purpose of this study is to examine the subwavelength behavior of the proposed absorber, the frequency below the QW of the longitudinal wave in the VE layer or below $f_{\lambda/4}$ is of interest. A normalized frequency of $\Omega = f/f_{\lambda/4}$ is used, where $f_{\lambda/4} = c_d/4h_1 = 2291.7$ Hz for a 6-cm-thick VE layer.

5.1. Verification of the results

Figure 2 compares the ACs of the VE layer with embedded PSs of two different widths and distances calculated by the DM and EMM, respectively. In Figs. 2(a) and (b), one can observe that, for a small PS width or $L = 0.04$ m, the AC calculated by the DM agrees well with that by the EMM for both small and large distances between the units of PSs. This is reasonable since the EMM assumes $\lambda_d/L >> 1$, while $\lambda_d \geq 0.24$ m $>> L$ holds within the entire frequency range of interest.

In Fig. 2(c), it is observed that, for wider PSs or $L = 0.09$ m and a smaller distance d, the AC calculated by the DM also matches very well with that by the EMM, and both match well with the results for embedded infinite PSs. From Fig. 2(d), as the distance d between the units of PSs decreases, the AC calculated by the DM gradually converges to that of the case with infinite PSs of the same number and thickness.

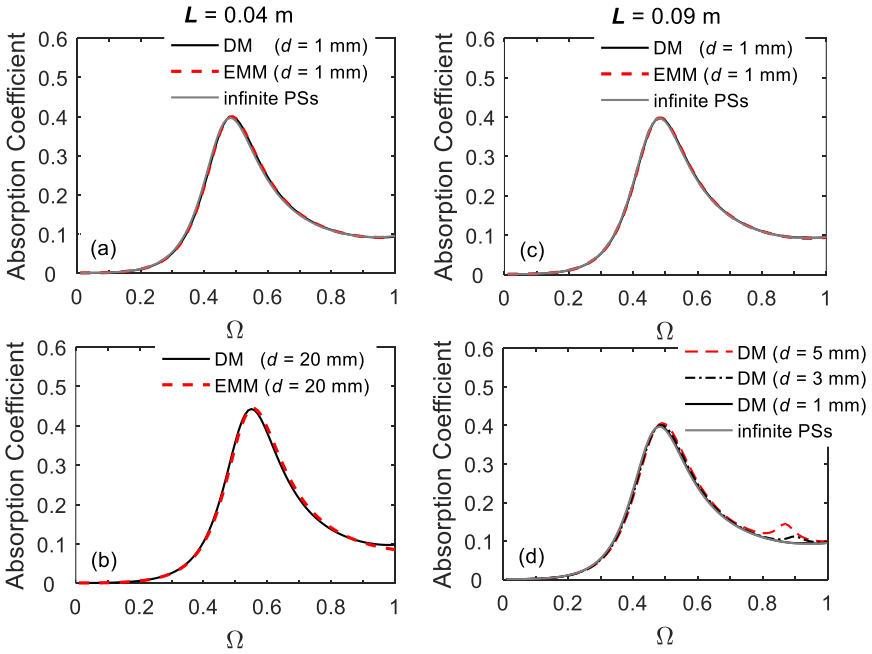

Fig. 2. Normal ACs of the VE layer with embedded PSs of infinite width and finite width calculated by different models.

For PSs of a larger size and a larger distances between the units of PSs, where the assumptions of EMM fail to hold, the FEM is used to validate the results predicted by the DM. Figure 3 shows the normal AC of the absorber for $L = 0.09$ m and $d = 0.06$ m. One can observe that the results based on the DM generally agree well with those predicted by the FEM. The

deviation between the results of the models can be attributed to neglecting the thickness of the PSs and the effect of higher-order plate waves in the PSs.

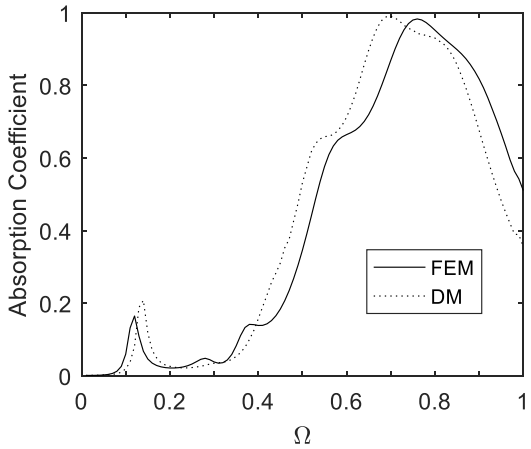

Fig. 3. Normal absorption coefficients of the proposed absorber with six embedded PSs in a unit cell, calculated by different models, with a solid curve for the FEM and a dotted curve for the DM with Δh = 0.1 m and h_{26} = 1 mm.

5.2. Multiband and broadband quasi-perfect sound absorption

Figure 4 compares the normal ACs with and without the embedded six PSs (I = 6) at various distances between the units of PSs. The width of each PS is fixed at L = 0.09 m. Without the embedded PSs (solid gray), a single absorption peak is observed at Ω = 1 or at the QW frequency as expected, because the water-loaded soft VE layer can be approximated as a rigid–free longitudinal waveguide (LW) or a QW resonator [25]. The AC thus reaches a maximum at the integer times of the QW frequencies.

With the embedded PSs and a longer distance between their units (d > 0.02 m), four AC peaks are observed below the QW frequency, denoted as P1, P2, P3, and P4. For d = 0.025 m, 0.03 m, and 0.04 m, quasi-perfect absorptions (over 93.0%) are observed at P1, P2, and P3 for layer thicknesses of 2.4%, 4.9%, and 5.8% of the wavelength of the incident sound (taking d = 0.04 m as an example). In addition, nearly full absorption (over 99.9%) is observed at P3 for d = 0.03 m, 0.04 m, and 0.05 m.

The frequencies and magnitudes of those AC peaks change as d is varied. Specifically, with increased d, the peak at P1 shifts to a lower frequency and the related AC slightly decreases; the frequency of P2 is hardly changed but its magnitude decreases when d > 0.03 m. The peaks at P3 and P4 both shift to higher frequencies as d increases, with the magnitude of P4 significantly increasing with d while that of P3 is hardly changed. Due to these variations of the AC peaks with d, a broadband quasi-perfect SA is observed near P2 and P3 for d = 0.02 m, 0.03 m, and 0.04 m, at a layer thickness of around 0.05 of the incident sound wavelength. Specifically, an AC over 98% and a bandwidth of 123.5 Hz are observed for d = 0.025 m, an AC over 99% and a bandwidth of 202 Hz for d = 0.03 m, and an AC over 95% and a bandwidth of 348.3 Hz for d = 0.04 m. When the distance d is increased to 0.05 m, an ultra-broadband quasi-perfect SA is even found near all P2, P3, and P4, with a related AC over 90% and a bandwidth of 572.9 Hz.

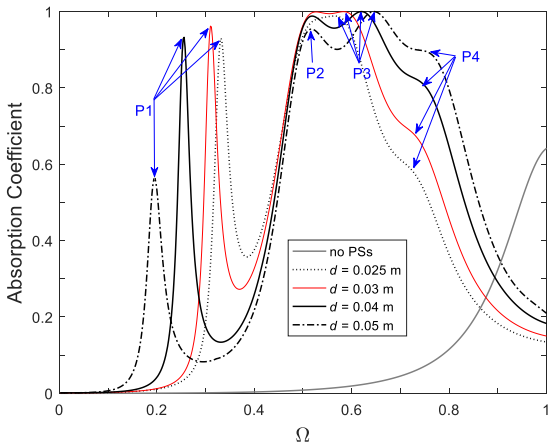

Fig. 4. Normal ACs from a viscoelastic layer with and without embedded PSs for various spaces between the units of PSs and L = 0.09 m.

5.3. Velocity fields and multiple LRs of different types

To find the physical origin of the quasi-perfect absorption at the above AC peaks, the velocity fields at the related frequencies of P1, P2, P3, and P4 are shown in Figs. 5(a), (b), (c), and (d) for L = 0.09 m and d = 0.04 m. For P1, the associated velocity field is strong around the middle parts of all the PSs but weak near their boundaries. From later observations in Fig. 7, this resonance frequency Ω_1 decreases with L but increases linearly with the PS's thickness h_{26}, so it can be inferred that the vibration at P1 is related to the bending motions of all the PSs with fixed boundaries. Bending resonance of a free–rigid boundary is also observed along the strip between units of PSs with a height of h_1 and a width of d, which is also supported by observations in Figs. 4, 6, and 7 that the frequency related to P1 decreases with d but increases with h_1. The quasi-perfect absorption at P1 is thus attributed to resonant excitations of multiple local bending modes of the PSs and those between units of PSs. Note that the origin of this peak is different from that of its counterpart in Ref. [25], which stems from a combined effect of the locally resonant bending modes of the PSs and the locally resonant LW mode between units of PSs.

For P2, as shown in Fig. 5(b), the vibration is mainly concentrated between the 6th PS and the water–layer interface. From the previous results in Fig. 4 and those in Fig. 7, the frequency of P2 hardly changes with d, but increases linearly with L, declines with h_2, and drastically declines with h_1. It thus can be inferred that the quasi-perfect absorption at P2 arises mainly from resonant excitation of local bending modes of the layer region between the 6th PS and the water–layer interface and with a height of L and a length of $h_1/7$.

For P3, as shown in Fig. 5(c), besides the concentrated vibration between the 6th PS and the water–layer interface, strong velocity is also found between the units of PSs and is stronger near the bottom of the layer. From Fig. 7, the related frequency increases linearly with d, but decreases drastically with L and h_1, so the vibration between the units of PSs can be interpreted as a local free–fixed bending mode with a height of d and a length of h_1, while that between the 6th PS and the water–layer interface is a local LW mode with a height of $2h_1/7$ and a length of L. Consequently, the quasi-perfect absorption at P3 stems from resonant excitations of local LW modes between the 6th PS and the water–layer interface and local

bending modes between the units of PSs.

For P4, as shown in Fig. 5(d), strong vibration is not only observed between the 6th PS and the water–layer interface and between the units of PSs near the bottom of the layer with a height of $2h_1/7$, it is also found near and between the PSs in a unit. From Fig. 7, the frequency of P4 decreases with L and h_1 but increases with d and h_2, so one can infer that the SA peak at P4 arises from the resonant excitations of local bending modes of the PSs in a unit and between the units of PSs with a height of d and a length of $2h_1/7$, together with the local LW modes between the $(i+1)$th PS and the ith PS/the water–layer interface in a unit.

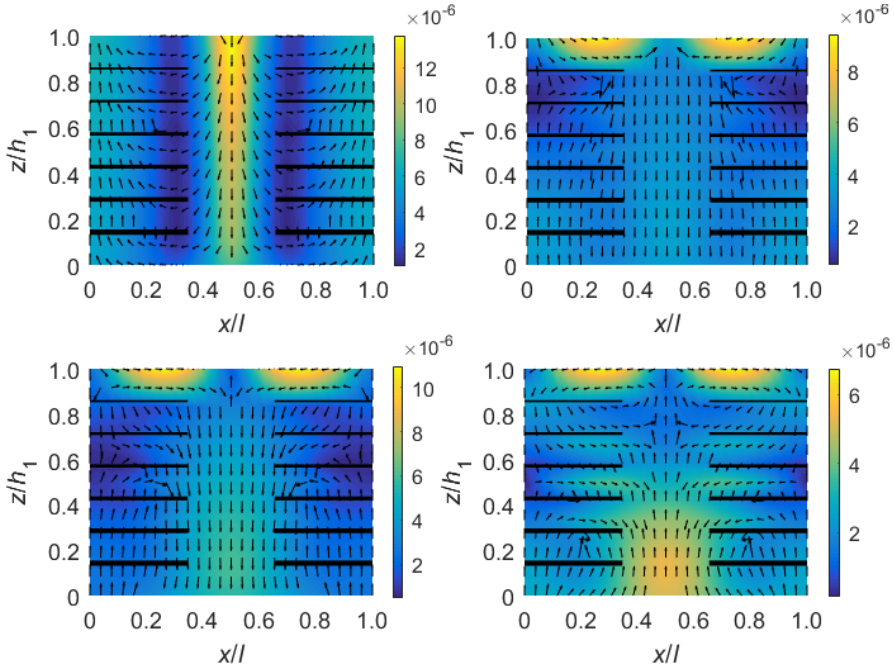

Fig. 5. Velocity field distributions in the viscoelastic layer with embedded PSs at the frequencies related to P1, P2, P3, and P4, or at (a) $\Omega = 0.256$, (b) $\Omega = 0.518$, (c) $\Omega = 0.620$, and (d) $\Omega = 0.742$, respectively, for $L = 0.09$ m and $d = 0.04$ m.

5.4. Parameter analysis

To further investigate the effects of the other parameters of the PSs and VE layer on the SA properties of the absorber, Figs. 6(a)–(e) show the variation of the normal AC with the width, thickness, and thickness gradient of the PSs, the thickness of the VE layer, and the loss factors in the layer, respectively, with $L = 0.09$ m and/or $d = 0.04$ m.

As shown by Fig. 6(a), as L increases, the resonance frequencies of the SA at P1, P3, and P4 decrease while the frequency of P2 increases. In addition, the AC at P4 also increases significantly with L. As a result, an ultra-broadband quasi-perfect SA is observed for $L = 0.08$ m in the vicinity of P2, P3, and P4, with a related AC over 83.7% and a bandwidth of 751.7 Hz.

Figure 6(b) demonstrates that the magnitudes of the AC at P1, P3, and P4 all generally decrease as h_{2i} decreases. Meanwhile, the resonance frequencies at P1, P3, and P4 decrease, while that at P2 increases. Figure 6(c) shows that the larger the thickness gradient Δ_h between adjacent PSs in a unit, the higher the magnitudes and resonance frequencies of P1 and P4 will be, and the lower the frequencies of P2 will be. Meanwhile, the magnitudes of P1, P2, and P4 all increase with Δ_h, while that of P3 increases for $\Delta_h \leq 0.1$ mm but decreases for $\Delta_h > 0.1$ mm.

The relations between these resonance frequencies, or Ω_1, Ω_2, Ω_3, and Ω_4, and the geometric parameters of the absorber, namely L, d, h_{2i}, and h_1, are shown in Fig. 7.

The effects of the loss factors related to the shear waves and dilatational waves in the layer are shown in Figs. 6(e) and (f), respectively. In general, the larger the shear loss factor, the broader the bandwidth of all four peaks will be. Comparatively, the dilatational loss factor has only a slight effect on the SA peaks, especially for P1.

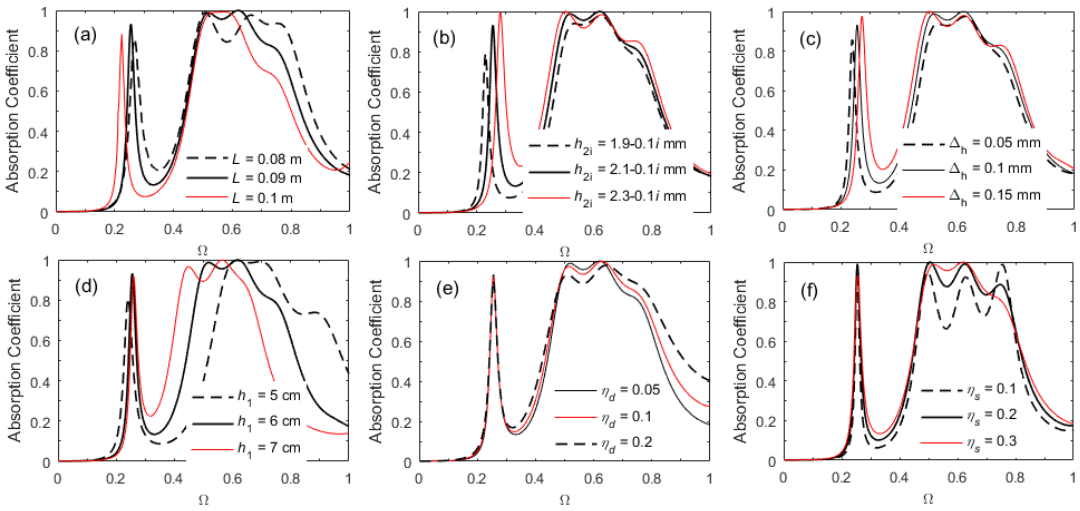

Fig. 6. Absorption coefficients of the proposed absorber at different (a) PS widths L, (b) PS thicknesses h_{2i}, (c) thickness gradient Δh, (d) layer thicknesses h_1, (e) layer dilatational loss factors η_d, and (f) layer shear loss factors η_s, with L = 0.09 m and/or d = 0.04 m.

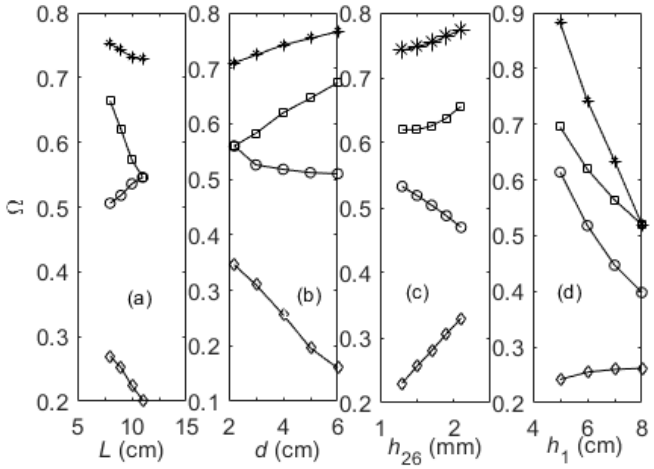

Fig. 7. Dependence of the resonance frequencies of P1 (diamond), P2 (circle), P3 (square), and P4 (star) on the geometric parameters of the proposed absorber, with (a) width, (b) distance between units of PSs, and (c) thickness of the 6th PS, and (d) layer thickness.

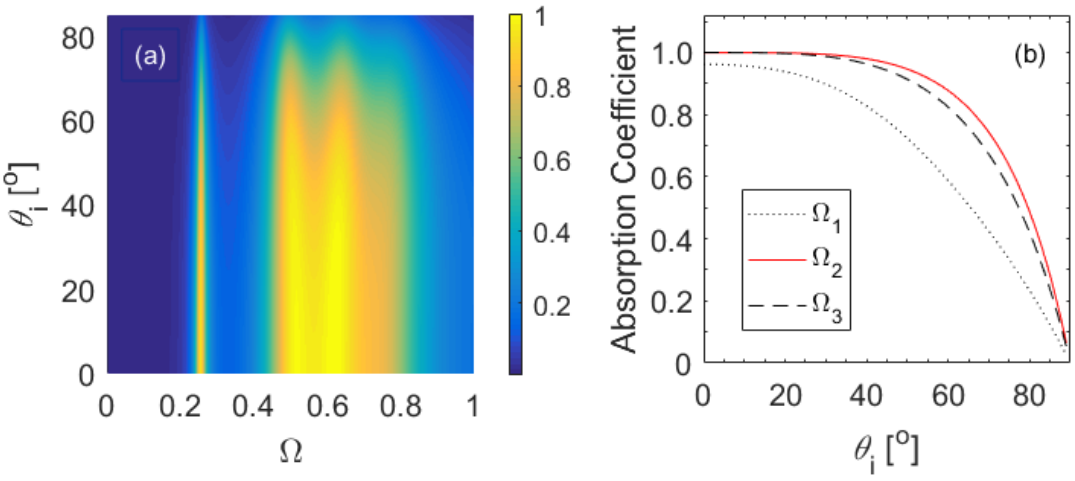

Fig. 8. Absorption coefficients of the proposed absorber for sound waves at different incidence angles, when L = 0.09 m and d = 0.03 m.

Figure 8(a) shows the ACs of the proposed absorber at various incidence angles when L = 0.09 m and d = 0.03 m. A perfect absorption (100%) occurs at θ_i = 12°, 13°, and 14° near the frequency of P3, or at Ω = 0.622. For the peaks of P1, P2, and P3, the angle ranges for ACs larger than 0.9 are $\theta_i \leq$ 27°, 56°, and 55°, and those for ACs larger than 0.8 are $\theta_i \leq$ 48°, 66°, and 64°, respectively, which can be easier identified from Fig. 8(b). These perfect/quasi-perfect SAs near the aforementioned four peaks have little angular dependence for a broad range of incidence angles, despite a slight shift of their resonance frequencies. The weak angular dependence is expected, since these high or quasi-perfect absorptions all originate from resonant excitations of the intrinsic local modes inside the layer. The proposed ultrathin quasi-perfect absorber thus also displays a quasi-omnidirectional behavior.

5. Conclusions

In this study, an ultra-thin sound absorber made up of a thin viscoelastic (VE) layer embedded with periodically distributed plate scatterers (PS) was proposed for the efficient absorption of low-frequency broadband underwater sound. Compared with the very low absorption of the VE layer without embedded PSs, quasi-perfect sound absorptions (SA) were observed at four resonance frequencies below the quarter-wavelength (QW) frequency, due to the introduced PSs. These quasi-perfect SAs stem from resonant excitations of multiple local modes of different types inside the absorber. These local modes include not only local bending modes of the PSs, between the units of PSs and between the Ith PS and the water–layer interface, but also local longitudinal waveguide modes between units of PSs, between the Ith PS and the water–layer interface, and between PSs in a unit. Broadband low-frequency sound absorption can be realized by the combined effect of these local resonance modes via proper adjustment of the width, thickness of each PS, the thickness gradient between PSs, and the space between PSs in a unit or between the units of PSs, and by a higher shear loss factor. Quasi-perfect absorption behavior is also maintained for a wide range of incident angles. Compared with the previous absorber design in Ref. [25], the current absorber exhibits better low-frequency SA performance and is easier to fabricate. It thus offers a simpler and effective

method for developing an ultrathin underwater sound absorber with broadband and omnidirectional absorption properties.

Acknowledgments

The project was supported by the National Science Foundation of China (Grant Nos. 11874304 and 11504324), and the Natural Science Basic Research Plan in Shaanxi Province of China (Program No. 2018JQ1001). This work was also supported by the Fundamental Research Funds for the Central Universities (No. 3102017OQD008).

Appendix: Related formulae and equations for the DM

The nonzero entries of $[\mathrm{F}_{n,q-n}]$ in Eq. (16) are given by:

$$f_{4r-1,4r-3} = g_{(r-1)R1}c_{q-n} + s_{(r-1)R1}Z_{r,fq,n}c_{q-n}, \tag{A1}$$

$$f_{4r-1,4r-2} = g_{(r-1)R2}c_{q-n} + s_{(r-1)R2}Z_{r,fq,n}c_{q-n}, \tag{A2}$$

$$f_{4r-1,4r-1} = g_{(r-1)R3}c_{q-n} + s_{(r-1)R3}Z_{r,fq,n}c_{q-n}, \tag{A3}$$

$$f_{4r-1,4r} = g_{(r-1)R4}c_{q-n} + s_{(r-1)R4}Z_{r,fq,n}c_{q-n}, \tag{A4}$$

$$f_{4r-1,4r+1} = g_{(r-1)R1}c_{q-n}, \tag{A5}$$

$$f_{4r-1,4r+2} = g_{(r-1)R2}c_{q-n}, \tag{A6}$$

$$f_{4r-1,4r+3} = g_{(r-1)R3}c_{q-n}, \tag{A7}$$

$$f_{4r-1,4r+4} = g_{(r-1)R4}c_{q-n}, \tag{A8}$$

$$f_{4r,4r-3} = \left(s_{(r-1)R5} + g_n s_{(r-1)R1}\right)Z_{r,lq,n}c_{q-n}, \tag{A9}$$

$$f_{4r,4r-2} = \left(s_{(r-1)R6} + g_n s_{(r-1)R2}\right)Z_{r,lq,n}c_{q-n}, \tag{A10}$$

$$f_{4r,4r-1} = \left(s_{(r-1)R7} + g_n s_{(r-1)R3}\right)Z_{r,lq,n}c_{q-n}, \tag{A11}$$

$$f_{4r,4r} = \left(s_{(r-1)R8} + g_n s_{(r-1)R4}\right)Z_{r,lq,n}c_{q-n}, \tag{A12}$$

$$f_{4r+2,4r-3} = 2g_{r,n}s_{(r-1)R1}c_{q-n}, \tag{A13}$$

$$f_{4r+2,4r-2} = 2g_{r,n}s_{(r-1)R2}c_{q-n}, \tag{A14}$$

$$f_{4r+2,4r-1} = 2g_{r,n}s_{(r-1)R3}c_{q-n}, \quad \text{and} \tag{A15}$$

$$f_{4r+2,4r} = 2g_{r,n}s_{(r-1)R4}c_{q-n}, \tag{A16}$$

where $g_{rR1} = g_{r+1,ran}\sin(r\alpha_n h_{c1})$, $g_{rR2} = -g_{r+1,ran}\cos(r\alpha_n h_{c1})$, $g_{rR3} = -g_{r+1,n}R_{1n}\cos(r\beta_n h_{c1})$, and $g_{rR4} = -g_{r+1,n}R_{1n}\sin(r\beta_n h_{c1})$, with $g_{r,ran} = g_{r,n}R_{2n}\alpha_n$ and $g_{r,n} = \frac{jk_n h_{2r}}{2}$; s_{rRt}, $t = 1,2,...8$ are equivalent to their counterparts in Ref. [25], for r = 1, 2, …, I; and $Z_{r,fq,n} = (D_2 k_n^2 k_q^2 - \rho_2 h_{2r}\omega^2)$, $Z_{r,lq,n} = E_2^{'} h_2 k_n k_q - \rho_2 h_{2r}\omega^2$.

References

[1] J. Mei, G. Ma, M. Yang, Z. Yang, W. Wen, P. Sheng, Dark acoustic metamaterials as super absorbers for low-frequency sound, Nat. Commun. 3 (2012) 756.

[2] Y.R. Wang, X.H. Miao, H. Jiang, M. Chen, Y. Liu, W.S. Xu, D. Meng, Review on underwater sound absorption materials and mechanisms. Advances in Mechanics, 47 (2017) 201703.

[3] J.P. Groby, W. Huang, A. Lardeau, Y. Aurégan, The use of slow waves to design simple sound absorbing materials. J. Appl. Phys. 117 (2015) 124903.

[4] J.S. Sastry, M.L. Munjal, A transfer matrix approach for evaluation of the response of a multi-layer infinite plate to a two-dimensional pressure excitation, J Sound Vib. 182 (1995) 109–128.

[5] H. Zhao, J. Wen, H. Yang, L. Lv, X. Wen, Backing effects on the underwater acoustic absorption of a viscoelastic slab with locally resonant scatterers, Appl. Acoust. 76 (2014) 48–51.

[6] H. Meng, J. Wen, H. Zhao, L. Lv, X. Wen. Analysis of absorption performances of anechoic layers with steel plate backing, J. Acoust. Soc. Am. 132 (2012) 69–75.

[7] S. Beretti, M. Vassas, Multifunction coating (anechoic-decoupling) and enhanced anechoic coating by using multiplayer optimization, Conference Proceedings UDT. London, (1996) 300–303.

[8] S.M. Ivansson, Sound absorption by viscoelastic coatings with periodically distributed cavities, J. Acoust. Soc. Am. 119 (2006) 3558–3567.

[9] S.M. Ivansson, Numerical design of Alberich anechoic coatings with superellipsoidal cavities of mixed sizes, J. Acoust. Soc. Am. 124 (2008) 1974–1984.

[10] W. Xu, C. Jiang, J. Zhang, Improvement in underwater acoustic absorption performance of open-celled SiC foam, Colloid Surface A. 482 (2015) 568–574.

[11] H. Jiang, Y. Wang, Phononic glass: A robust acoustic-absorption material, J. Acoust. Soc. Am. 132 (2012) 694–699.

[12] Z. Liu, X. Zhang, Y. Mao, Y. Y. Zhu, Z. Yang, C.T. Chan, P. Sheng, Locally resonant sonic materials, Science, 289 (2000) 1734–1736.

[13] H. Zhao, J. Wen, D. Yu, X. Wen, Low-frequency acoustic absorption of localized resonances: experiment and theory, J. Appl. Phys. 107 (2010) 1–5.

[14] J. Wen, H. Zhao, L. Lv, B. Yuan, G. Wang, X. Wen, Effects of locally resonant modes on underwater sound absorption in viscoelastic materials, J. Acoust. Soc. Am. 130 (2011) 1201–1208.

[15] H. Meng, J. Wen, H. Zhao, X. Wen, Optimization of locally resonant acoustic metamaterials on underwater sound absorption characteristics, J. Sound Vib. 331 (2012) 4406–4416.
[16] Y. Xiao, J. Wen, X. Wen, Broadband locally resonant beams containing multiple periodic arrays of attached resonators. Phys. Lett. A. 376 (2012) 1384–1390.
[17] C.J. Naify, C. Chang, G. McKnight, S. Nutt, Transmission loss of membrane-type acoustic metamaterials with coaxial ring masses. J. Appl. Phys. 110 (2011) 124903.
[18] N. Jiménez, V. Romero-García, V. Pagneux, J.P. Groby, Quasiperfect absorption by subwavelength acoustic panels in transmission using accumulation of resonances due to slow sound, Phys. Rev. B. 95 (2017) 014205.
[19] H. Long, Y. Cheng, X. Liu, Asymmetric absorber with multiband and broadband for low-frequency sound, Appl. Phys. Lett. 111 (2017) 143502.
[20] J.P. Groby, R. Pommier, Y. Aurégan, Use of slow sound to design perfect and broadband passive sound absorbing materials, J. Acoust. Soc. Am. 139 (2016) 1660–1671.
[21] X. Wang , X. Luo, H. Zhao, Acoustic perfect absorption and broadband insulation achieved by double-zero metamaterials. Appl. Phys. Lett. 112 (2018) 021901.
[22] H. Long, Y. Cheng, J. Tao, X. Liu, Perfect absorption of low-frequency sound waves by critically coupled subwavelength resonant system, Appl. Phys. Lett. 110 (2017) 023502.
[23]Y. Li, B.M. Assouar, Acoustic metasurface-based perfect absorber with deep subwavelength thickness, Appl. Phys. Lett. 108 (2016) 204301,
[24] J. Mei, X. Zhang, Y. Wu, Ultrathin metasurface with high absorptance for waterborne sound, J. Appl. Phys. 123 (2018) 091710.
[25] Y. Zhang, J. Pan, K. Chen, Subwavelength and quasi-perfect underwater sound absorber for multiple and broad frequency bands, J. Acoust. Soc. Am, 2018 (in press).
[26] Y. Zhang, H. Huang, J. Zheng, J. Pan, Underwater sound scattering and absorption by a coated infinite plate with attached periodically located inhomogeneities, J. Acoust. Soc. Am, 138 (2015) 2707–2721.
[27] Y. Zhang, J. Pan, Enhancing acoustic signal response and absorption of an underwater coated plate by embedding periodical inhomogeneities, J. Acoust. Soc. Am. 142 (2017) 3722–3735.
[28] Y. Zhang, J. Pan, Underwater sound scattering and absorption by a coated infinite plate with a distributed inhomogeneity, Journal of the Acoustical Society of America, 133(2013), 2082–2096.
[29] M.C. Junger, D. Feit, Sound, Structures, and Their Interaction, 2nd ed. MIT, Cambridge, MA, 1986, pp. 236.
[30] J. Zhong, H. Zhao, H. Yang, J. Yin, J. Wen. Effect of Poisson's loss factor of rubbery material on underwater sound absorption of anechoic coatings. Journal of Sound and Vibration, 424 (2018) 293–301.